IJMMM International Journal of Minerals, Metallurgy and Materials 矿物冶金与材料学报（英文版）

Parametric study of spark plasma sintering of $Al_{20}Cr_{20}Fe_{25}Ni_{25}Mn_{10}$ high entropy alloy with improved microhardness and corrosion

Andries Mthisi, Nicholus Malatji, A. Patricia, I. Popoola, and L. Rudolf Kanyane

Cite this article as:
Andries Mthisi, Nicholus Malatji, A. Patricia, I. Popoola, and L. Rudolf Kanyane, Parametric study of spark plasma sintering of $Al_{20}Cr_{20}Fe_{25}Ni_{25}Mn_{10}$ high entropy alloy with improved microhardness and corrosion, *Int. J. Miner. Metall. Mater.*, 29(2022), No. 1, pp. 119-127. https://doi.org/10.1007/s12613-020-2200-3

International Journal of Minerals, Metallurgy and Materials
Volume 29, Number 1, January 2022, Page 119
https://doi.org/10.1007/s12613-020-2200-3

Parametric study of spark plasma sintering of $Al_{20}Cr_{20}Fe_{25}Ni_{25}Mn_{10}$ high entropy alloy with improved microhardness and corrosion

Andries Mthisi✉, *Nicholus Malatji*, *A. Patricia*, *I. Popoola*, *and L. Rudolf Kanyane*

Department of Chemical, Metallurgical and Materials Engineering, Tshwane University of Technology, P.M.B. X680, Pretoria, South Africa
(Received: 29 March 2020; revised: 16 September 2020; accepted: 20 September 2020)

Abstract: Multicomponent $Al_{20}Cr_{20}Fe_{25}Ni_{25}Mn_{10}$ alloys were synthesized using spark plasma sintering at different temperatures (800, 900, and 1000°C) and holding times (4, 8, and 12 min) to develop a high entropy alloy (HEA). The characteristics of spark plasma-synthesized (SPSed) alloys were experimentally explored through investigation of microstructures, microhardness, and corrosion using scanning electron microscopy coupled with energy dispersive spectroscopy (EDS), Vickers microhardness tester, and potentiodynamic polarization, respectively. X-ray diffraction (XRD) characterization was employed to identify the phases formed on the developed alloys. The EDS results revealed that the alloys consisted of elements selected in this work irrespective of varying sintering parameters. The XRD, EDS, and scanning electron microscopy collectively provided evidence that the fabricated alloys were characterized by globular microstructures exhibiting face-centered cubic phase, which was formed on a basis of solid solution mechanism. This finding implies that the SPSed alloy showed the features of HEAs. The alloy produced at 1000°C and holding time of 12 min portrayed an optimal microhardness of HV 447.97, but the value decreased to HV 329.47 after heat treatment. The same alloy showed an outstanding corrosion resistance performance. The increase in temperature resulted in an $Al_{20}Cr_{20}Fe_{25}Ni_{25}Mn_{10}$ alloy with superior density, microhardness, and corrosion resistance over the other alloys developed at different parameters.

Keywords: high entropy alloy; spark plasma sintering; microhardness; corrosion

1. Introduction

Numerous alloys have been developed for most engineering applications, but despite years of improvement, these alloys still exhibit limitations, such as low hardness and poor corrosion [1–2]. In 2004, a new class of material known as high entropy alloys (HEAs) with improved properties were developed. HEAs are centrally based on solid solution phases as a result of high entropy of mixing (ΔS_{mix}) induced by at least five or more elements, with each element content between 5at%–35at% [3]. Other effects, such as sluggish diffusion, severe lattice distortion, and cocktail effect, play important roles in determining the physical and mechanical properties of HEAs. On the other hand, conventional alloys comprise single elements as a solvent, whereas small traces of other elements are added as solutes [4]. Dissimilar to conventional alloys forming various phases due to the addition of alloying elements, HEAs form a simple single body-centered cubic (bcc) or face-centered cubic (fcc) solid solution [5]. Over 300 HEAs have been developed from 30 different elements [6]. Of the 30 considered elements, the HEAs developed from AlCoCrCuFeNi and AlCoCrMnFeNi possess high hardness depending on the elements' quantity [7]. The valence electron concentration (VEC) model proposed by Guo *et al*. [8] can predict the probability of bcc or fcc phase outcome on HEAs. Recent reports suggest that HEAs with the combination of bcc and fcc are desirable as these alloys exhibit balanced properties compared with singular bcc or fcc [5].

Liquid mixing, solid mixing, and gaseous mixing are methods commonly used to produce HEAs. However, liquid and gaseous techniques are regarded as costly because they involve intense heating and produce alloys with cracks. Spark plasma sintering technique (SPST), which falls under solid mixing, offers an option of producing HEAs with controlled grain size because no intense melting is involved [4,9]. To substantiate that SPST can be used to develop multicomponent alloys, Zhang *et al*. [10–11] prepared $CoSb_{2.79}Te_{0.16}Se_{0.05-x}S_x$ through this technique; meanwhile, Popescu *et al*. [12] reported that an equiatomic AlCrFeNiMn HEA can be fabricated through SPST given that the developed alloy exhibited fcc and bcc structures; however, the authors applied mechanical alloying (MA) on AlCrFeNiMn mixed powder prior to SPST. This procedure has become a common practice because MA enhances the formation of HEAs in nano-crystallines, which in turn lead to improved properties [13–14]. However, the rapid synthesis of alloys via SPST is retarded by prolonged times required to carry out MA [15].

SPST can guarantee the fabrication of HEAs with desired microstructures, with shortcomings brought about by MA be-

✉ Corresponding author: Andries Mthisi E-mail: Andriesmthisi@gmail.com

ing mitigated by using proper SPST parameters and utilizing gas-atomized element powder [16]. This statement can be justified by exploring the work of Kanyane *et al*. [4]; from their work they consolidated equiatomic TiAlMoSiW into HEA using SPST without employing MA on the premixed powder. However, in relation to AlCrFeNiMn, the fabrication of this alloy, particularly a non-equiatomic HEA, using SPST is sporadically reported. This study attempted to fabricate non-equiatomic $Al_{20}Cr_{20}Fe_{25}Ni_{25}Mn_{10}$ via SPST to develop HEA. Furthermore, comparisons of alloys fabricated at various sintering temperatures and holding times were performed to understand the relationship between SPST parameters and AlCrFeNiMn HEA properties.

2. Experimental

2.1. Powders and mixing

A non-equiatomic AlCrFeNiMn powder mixture was prepared using high-purity (99.5%) metal powders of Al, Fe, Ni, Cr, and Mn, with the particle size of powders ranging between 45 μm and 90 μm (TLS Technik GmbH & Co.). The powders were selected based on an earlier reported statement, that is, the development of non-equiatomic AlCrFeNiMn HEAs have been rarely developed using SPST. The appropriate mass ratio of each element powder determined by calculations using atomic ratios were weighted using an electronic scale and mixed together to attain a composition of 20%Al–20%Cr–25%Fe–25%Ni–10%Mn (at%). The premixed powder of AlCrFeNiMn was then subjected to mixing in dry state using a tubular mixer for 12 h at 49 $r \cdot min^{-1}$ to ensure homogenous distribution of the powders.

2.2. Sintering of mixed powders

A spark plasma sintering system (FCT Systeme GmbH Rauenstein) in a vacuum was used to consolidate the mixed powders of $Al_{20}Cr_{20}Fe_{25}Ni_{25}Mn_{10}$ (at%) at sintering temperatures of 800, 900, and 1000°C and holding times of 4, 8 and 12 min. SPST involves simultaneous powder pressing and heating, which is generated by a pulse direct current passing through an electric conducting graphite die filled with compacted powders. The rise in temperature, as a result of heating, causes the powders to bond and eventually yield a rigid dense alloy. Prior to sintering processing, the mixed powders were separately filled into a graphite die of 40 mm diameter and then loaded into the SPST machine. Under all considered sintering temperatures and holding times, the heating rate and applied pressure were kept constant at 100°C/min and 30 MPa.

2.3. Characterizations of spark plasma-synthesized (SPSed) alloy

2.3.1. Relative density

The densities of the fabricated alloys were measured by using the Archimedes' method. This method is based on the principle of submerging alloy specimens in deionized water filled in pycnometer volumetric flask surrounded by air. Archimedes' principle stipulates that the volume of specimen is equal to the volume of water if completely submerged. From here, the density can be determined. The averages of five readings were obtained for each specimen. The relative density of the sintered specimen was calculated as a fraction of the measured and theoretical densities.

2.3.2. Microstructure and phase characterizations

The fabricated alloys were sectioned mounted, grounded, and polished following standard metallographic procedure and etched in Kroll's reagent containing 92 mL distilled water, 6 mL nitric acid, and 2 mL hydrofluoric acid. The microstructural and elemental analyses of the synthesized alloys were examined by means of scanning electron microscopy (SEM) coupled with energy dispersive spectroscopy (EDS). The identification of phases evolved in the matrix of produced alloys were analyzed by X-ray diffraction (XRD; Philips Analytical X'Pert High Score VR software built-in with International Centre for Diffraction Data database).

2.3.3. Microhardness measurement

Microhardness property of the developed alloys was measured by using Vickers hardness tester (EMCOTEST) at a load of 980.66 N and with a dwell time of 10 s. Random indentations at five different positions were made onto the surface of each specimen, and the average was recorded and reported in Section 3.6. Microhardness test was carried out on SPSed alloys that were subjected to heat treatment. The heat treatment was performed at 800°C for 4 h and with sample cooling within the furnace.

2.3.4. Electrochemical measurements and surface morphology

The electrochemical behaviors of the developed alloys were studied using potentiodynamic polarization through a potentiostat (AUTOLAB PGSTAT30) device. The test was conducted using 1 cm^2 sample was submerged into a cell filled with 0.5 mol/L of H_2SO_4 solution and connected to the Autolab potentiostat. The cell was setup as follows. The solution composed 0.5 mol/L H_2SO_4 was used as the electrolyte at ambient temperature; three electrodes, namely, the working electrode (sample), counter electrode (platinum sheet), and silver/silver chloride electrode as a reference electrode (SCE), were connected. After the setup, a sample was cathodically polarized to a potential of −1.5 V for 5 s to remove the possibly existing surface oxides. The potentiodynamic test was then performed at a scan rate of 0.001 mV/s from an initial potential of −0.8 to final potential of 0.5 V. As corrosion commenced, the potentiodynamic polarization curve was plotted by NOVA software integrated with a potentiostat. Immediately after corrosion testing, the surface morphology of the corroded sample was investigated using SEM.

3. Results and discussion

3.1. Calculations

Table 1 presents the calculated values of mixing enthalpy (ΔH_{mix}) and ΔS_{mix} of the developed $Al_{20}Cr_{20}Fe_{25}Ni_{25}Mn_{10}$ alloy. Table 1 also shows other parameters, such as parameter

Ω and atomic size difference, which define the feasibility of solid solution formation, as referred from the work of Kanyane *et al.* [4]. The solid solution phases form when the critical parameters, i.e., ΔH_{mix}, δ, and ΔS_{mix}, are in the following ranges: $0 \le \delta \le 8.5$, $-22 \le \Delta H_{mix} \le 7$ kJ·mol^{-1}, $11 \le \Delta S_{mix} \le 19.5$ J·K^{-1}·mol^{-1}, and $\Omega \ge 1.1$ [5,9]. These parameters were determined by the models described in Eqs. (1), (2), (4), and (5).

$$\Delta S_{mix} = -R\sum_{i=1}^{n} C_i \ln C_i \quad (1)$$

where C_i, n, and R are the atomic fraction of the components, the number of elements in an alloy system, and gas constant (8.314 J·K^{-1}·mol^{-1}), respectively.

$$\Delta H_{mix} = \sum_{i=1}^{n} \Omega_{ij} C_i C_j \quad (2)$$

$$\Omega_{ij} = 4\Delta H_{AB}^{mix} \quad (3)$$

The constituents in Eq. (2) are defined as the Ω_{ij} that represents the regular solution parameter interaction between *i*th and *j*th elements; the parameter can be determined through the ΔH_{mix} of binary liquid alloys on the basis of Miedema's principle [4].

$$\Omega = \frac{T_m \Delta S_{mix}}{\Delta H_{mix}} \quad (4)$$

$$T_m = \sum_{i=1}^{n} C_i (T_m)_i \quad (5)$$

The average melting temperature (T_m) of the HEA can be calculated using the mixing variable in Eq. (5).

$$\delta = 100\sqrt{\sum_{i=1}^{n} C_i \left(1 - \frac{r_i}{r}\right)^2} \quad (6)$$

$$r = \sum_{i=1}^{n} C_i r_i \quad (7)$$

where r_i is the atomic radius of the *i*th element [9].

Table 1. Calculated values of (ΔH_{mix}, ΔS_{mix}, T_m, δ, and Ω) parameters for the $Al_{20}Cr_{20}Fe_{25}Ni_{25}Mn_{10}$ alloy

ΔH_{mix} / (kJ·mol^{-1})	ΔS_{mix} / (J·K^{-1}·mol^{-1})	δ / %	Ω	T_m / K
−12.46	13.03	0.35	1.7	1659.3

The above-mentioned parameters determined herein were within the ranges proposed in literature. Furthermore, the solid solution phases can be formed at any temperature in accordance with the Gibbs free energy equation (Eq. 8). However, the chances of phase formation increased as temperature increased.

$$\Delta G_{mix} = \Delta H_{mix} - T\Delta S_{mix} \quad (8)$$

The VEC of an alloy is another parameter apart from the strong atomic size effect and electronegativity that constitute the crystallinity of a solid solution phase according to the Hume–Rothery rule [17]. The model from the work of Guo *et al.* [8] illustrates that fcc or bcc forms when VEC > 7.92 or VEC < 6.8, respectively. VEC values between 6.8 and 7.92 yield a combined bcc and fcc structure [8,18]. This parameter is calculated using the model proposed by Guo *et al.* [8] (Eq. 9). Herein, VEC was applied to determine whether the predicted phases correlated with the formed phases on the SPSed alloys despite the varying sintering parameters. The calculated average VEC of $Al_{20}Cr_{20}Fe_{25}Ni_{25}Mn_{10}$ was 7 (Table 2), and this value indicates that the alloy should be composed of fcc and bcc phases. The VEC of $Al_{20}Cr_{20}Fe_{25}Ni_{25}Mn_{10}$ alloy was within the range of 6.8–7.92, with Al, Mn, and Cr accounting for 50% of the total atomic composition of the alloy. Aluminum had the lowest VEC. Thus, the high content of Al lowered the overall VEC of the alloy. On the other hand, 50% of the total content of the alloy was constituted by Fe and Ni, with the latter portraying the highest VEC (Table 2). As witnessed by Munitz *et al.* [19] the presence of Al at high contents in high-VEC alloys leads to fcc to bcc transformation, which implies a decline in VEC. Choudhuri *et al.* [20] observed that an Al content of as much as 12at% significantly influences the transition from fcc to bcc phase. Herein, Al quantity approximated 20at%. Thus, the probability of transformation due to Al was amplified. The presence of different crystalline structures prompts the formation of grain boundaries due to mismatch. Experimental work was performed to verify whether these predictions transpired, and the characterization results are reported in Sections 3.3 and 3.5.

$$\mathrm{VEC} = \sum_{i=1}^{n} C_i (\mathrm{VEC})_i \quad (9)$$

Table 2. VEC calculation of $Al_{20}Cr_{20}Fe_{25}Ni_{25}Mn_{10}$ alloy

Element	VEC	Composition / at%	Average VEC of the alloy
Al	3	20	7.00
Cr	6	20	
Mn	7	10	
Fe	8	25	
Ni	10	25	

3.2. Density analysis

Fig. 1 shows the densification of $Al_{20}Cr_{20}Fe_{25}Ni_{25}Mn_{10}$ alloy at varied sintering temperatures of 800, 900, and 1000°C and holding times of 4, 8, and 12 min. From Fig. 1, the sintering temperature and holding time of 1000°C and 12 min, respectively, yielded an alloy with an optimum apparent dens-

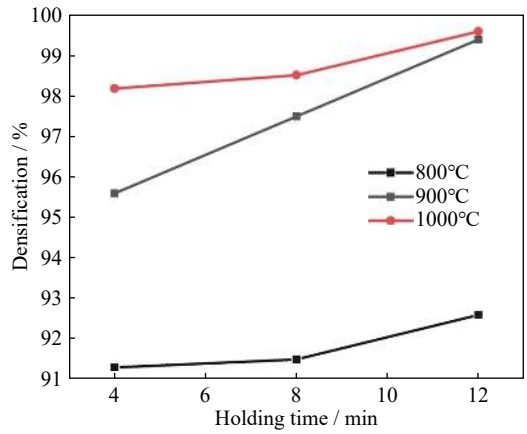

Fig. 1. Densification results of $Al_{20}Cr_{20}Fe_{25}Ni_{25}Mn_{10}$ sintered alloys.

ity of 99.6% of the theoretical density.

On the other hand, the lowest apparent densification of 91.3% of theoretical density was observed in the alloy developed at the sintering temperature of 800°C and 8 min holding time. Comparatively, the sintering temperature showed more effect on the densification of $Al_{20}Cr_{20}Fe_{25}Ni_{25}Mn_{10}$ alloy over holding time. This observation was attributed to the increase in temperature support powders that approached that of liquid sintering, which led to the fabrication of dense alloy [21]. However, despite showing less influence compared with temperature, the holding time increased the alloy density. This manifestation can be determined by considering the literature indicating that holding time plays a role in homogenous solid solution formation [22]. Solid solutioning of phases illustrates that atoms of different elements in the premixed powder diffused subsequently, inducing the formation of a dense alloy.

3.3. Microstructures

Fig. 2(a)–(b) shows the SEM micrographs of $Al_{20}Cr_{20}Fe_{25}Ni_{25}Mn_{10}$ alloy sintered at 800 and 1000°C, respectively, with a holding time of 12 min. Fig. 3(a)–(c) presents the micrographs of $Al_{20}Cr_{20}Fe_{25}Ni_{25}Mn_{10}$ alloy fabricated at 1000°C at various holding times of 4, 8, and 12 min, respectively. The micrographs of all samples revealed no significant presence of pores and cracks.

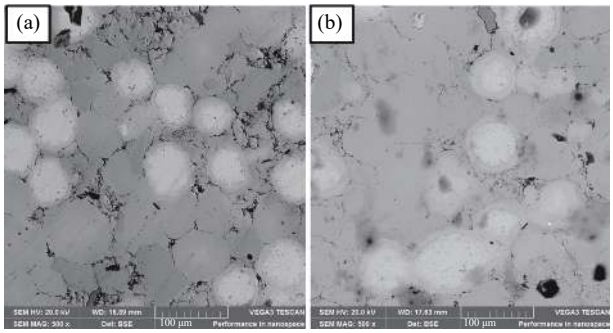

Fig. 2. SEM micrographs of $Al_{20}Cr_{20}Fe_{25}Ni_{25}Mn_{10}$ sintered alloys at 12 min holding time and temperatures of (a) 800 and (b) 1000°C.

The absence of such defects illustrates that all the parameters selected for sintering the studied alloy achieved high densification (Fig. 1). However, the samples fabricated at 1000°C showed traces of cavities in comparison with their counterparts. The cavities were pronounced (Fig. 3(b)–(c)) and might have resulted from the increase in holding time at 1000°C. Fig. 3(a)–(c) also shows that the grain size of $Al_{20}Cr_{20}Fe_{25}Ni_{25}Mn_{10}$ alloy increased with holding time and temperature increments. Cavity formation in relation to increase in holding time at 1000°C transpired possibly due to the prolonged holding time, which allowed the burning of low-melting-point elements, such as Al, from the alloy system because of high pressure and temperature [4]. The increased grain size because of holding time increment was ascribed to the sufficient time for grain growth, thereby reducing boundaries before being cooled below the recrystallization temperature, as also reported in literature [23]. Meanwhile, grain coarsening due to the increase in sintering temperature was expected given the common grain growth law, which can be found in the work of Wagner *et al.* [24].

The structures shown in Figs. 2(a)–(b) and 3(a)–(c) were globular for all the present phases. Herein, the observation of globular microstructures in the SPSed alloy can be referred to the findings of Kennedy *et al.* [25]. The explanation behind the globular microstructure formation is related to the solute or thermal instabilities, which are unable to progress [26]. SPST does not induce complete melting, implying that the alloys synthesized in this work at the average melting point presented in Table 1 (1659.3 K) were exposed to low temperatures during sintering. Despite their low values, these sintering temperatures were higher than the melting temperature of Al, and this condition prompted liquid particle (Al) fusion with existing solid crystals, leading to the formation of globular microstructures. This mechanism was also reported by the results of Adedayo [26]. However, given the number of grains present in the microstructures, diffusion was not only achieved by Al atoms. During sintering, diffusion of elements was also activated by the combined events of spark discharge, joule heating, electric field, powder rearrangement, and plastic deformation at temperature above $0.6T_m$ (melting temperature of a material) [21,27].

Four distinctive phases can be distinguished as white, light gray, gray, and dark phases from Figs. 2(a)–(b) and 3(a)–(c). Table 3 shows the results of quantitative volume analysis of these above-mentioned phases in the SPSed alloy matrix.

Table 3 shows that the gray phase was prominent in all the alloys. The volume fraction of the gray phase increased with the increase in holding time, whereas the increase in temperature showed a non-distinctive trend. Thus, the gray phase was probably the solid solution crystal occupying most of the

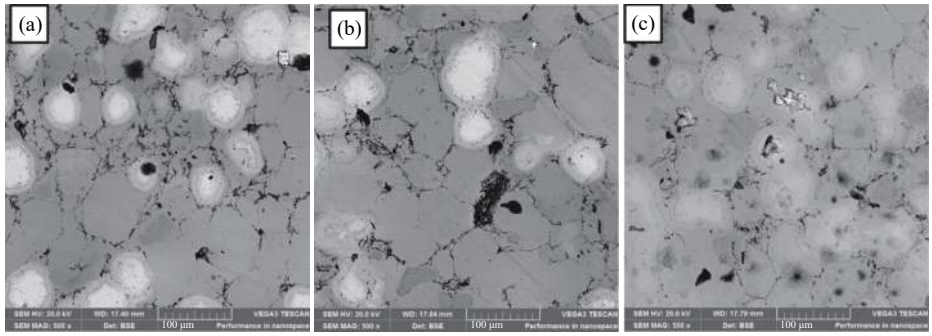

Fig. 3. SEM micrographs of $Al_{20}Cr_{20}Fe_{25}Ni_{25}Mn_{10}$ sintered alloys at 1000°C with holding time of (a) 4, (b) 8, and (c) 12 min.

Table 3. Volume of fraction of phases present in SPSed alloys displayed in Figs. 2 and 3

Figure	White phase / vol%	Gray phase / vol%	Dark phase / vol%
Fig. 2(a)	16.5	69.8	13.7
Fig. 2(b)	32.1	49.91	17.6
Fig. 3(a)	20.8	63.9	15.3
Fig. 3(b)	11.7	78.14	10.16
Fig. 3(c)	1.08	89.64	9.28

SPSed alloy matrix, and its formation intensified when the interaction of elements within the matrix was prolonged due to the increase in sintering holding time. Meanwhile, other phases formed at low volume quantities because most elements favorably participated in the gray phase formation. The EDS analysis further gave evidence of the elements constituting each phase.

3.4. EDS analysis

The distinctive phases observed in the microstructures reported in Section 3.2 were quantified by using EDS. Fig. 4 presents the elemental content results in relation with the phases. The light gray (spectrum 5) and gray phases (spectrum 1) were Fe-rich and Cr-rich grains, respectively. The white phase (spectrum 2) was predominated by Ni atoms. Meanwhile, dark phase (spectrum 3) was composed of Al. Noticeably, the Fe-rich phase (light gray) was dominant in all the microstructures, implying that most elements in minor quantity (Al, Cr, and Mn) successfully diffused into the Fe and Ni lattice structures, respectively, regardless of the varying sintering parameters. XRD was employed to define the crystal structure of the phase that dominated the microstructures of the developed alloy, and the results are divulged in Section 3.5.

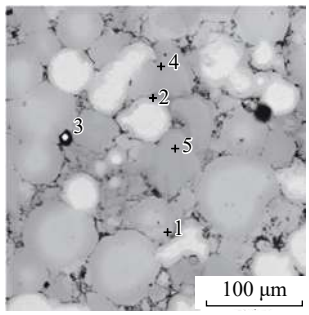

Spectrum	Atomic fraction / %				
	Fe	Mn	Al	Cr	Ni
1	80	10	9.46	0.54	0
2	2.31	3.37	14.32	0	80
3	0	0	56.8	43.2	0
4	0	0	0	100	0
5	0	0	0	100	0

Fig. 4. SEM/EDS micrographs of $Al_{20}Cr_{20}Fe_{25}Ni_{25}Mn_{10}$ sintered alloy at 800°C and holding time of 12 min.

3.5. Phase constituents

Fig. 5 shows the XRD patterns of $Al_{20}Cr_{20}Fe_{25}Ni_{25}Mn_{10}$ alloy sintered at 800, 900, and 1000°C with a holding time of 8 min. The XRD showed that the alloy phases were composed of the elements used in this work. As shown in Fig. 5, all the XRD patterns of the alloys revealed a fcc phase detected as a major peak at 45°. In addition, the XRD diffractograms showed the scattering of bcc phase and AlCr at 43° and 52° respectively, whereas a minor AlNi intermetallic phase was detected at 78°. In relation to microstructures, the major peak correlated to the gray phase, which was pronounced in the microstructures shown in Figs. 2(a)–(b) and 3(a)–(c). This finding can be substantiated with reference to the work of Elkatatny *et al.* [28]; the authors showed that the $Al_5Cr_{12}Fe_{35}Mn_{28}Ni_{20}$ alloy portrayed the fcc phase as a major peak at 45° and contained high Fe content. On the other hand, phases that included bcc, AlCr, and AlNi intermetallics corresponded to the other phases that appeared in the microstructures. The presence of fcc as a major phase signified the formation of solid solution in spark plasma-sintered (SPS) $Al_{20}Cr_{20}Fe_{25}Ni_{25}Mn_{10}$ alloy. Thus, the $Al_{20}Cr_{20}Fe_{25}Ni_{25}Mn_{10}$ formed a HEA. The formation of solid solution can be explained in the following manner. First, thermodynamic parameters (Table 1), such as enthalpy of mixing (ΔH_{mix}), entropy of mixing (ΔS_{mix}), and atomic size difference (δ), suggest that $Al_{20}Cr_{20}Fe_{25}Ni_{25}Mn_{10}$ alloy can form a solid solution phase irrespective of the varying sintering parameters as stated in Section 3.1.

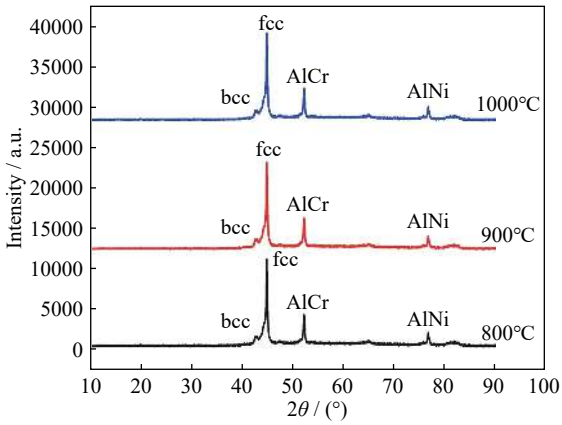

Fig. 5. XRD spectrum of $Al_{20}Cr_{20}Fe_{25}Ni_{25}Mn_{10}$ alloy sintered at 800, 900, and 1000°C at a holding time of 8 min.

The high ΔS_{mix} induced by the presence of numerous elements in a system suppresses the potential formation of intermetallic compounds formed mostly by two elements [29]. Based on the calculated VEC value (Table 2), the $Al_{20}Cr_{20}Fe_{25}Ni_{25}Mn_{10}$ HEA should have been composed of fcc and bcc. Given such argument, bcc is strongly associated with the diffusion between Al and Cr [30]. Herein, both intermetallic phases detected recompensed bcc although simple bcc is regarded as a solid solution phase. Furthermore, the calculated VEC of 7 slanted toward the direction of fcc phase precipita-

tion compared with the bcc that formed at VEC < 6.8. Meanwhile, the AlNi intermetallic formed because the mixing enthalpies of Ni and Al were substantially lower (more negative) than those of the other elements present in the matrix (Cr, Fe, and Mn) [8]. Al and Ni atoms formed an intermetallic compound due to their high negative ΔH_{mix} [31]. The competition between entropy and enthalpy explains why the interaction of other elements did not yield intermetallics. The low ΔH_{mix} between element pairs indicated a high entropy, which supports the solid solution formation. On the other hand, AlCr precipitated as an intermetallic because of Al diffusion into Cr due to high electronegativity, and the intermetallic of these elements is a stable low-entropy compound [32]. However, intermetallics formed in low intensity due to the presence of numerous elements in the matrix, which induced high ΔS_{mix}, thereby forming a solid solution. The fcc solid solution formed because of the presence of numerous elements that are fcc in nature. However, as reported in sub-Section 3.1, the addition of Al initiated the transformation of fcc to bcc.

Additionally, for the sintering temperature, the increase from 800 to 900 and 1000°C caused no changes in the phase constituents, phase shifts, and phase intensities of the SPSed alloys. Sintering temperature induces the rapid diffusion of elements [22]. This condition means that the phase intensities should have increased with the temperature increase. However, this event could not occur possibly because 8 min of sintering holding time was adequate to ensure phase transformation, thus reducing the intensity of fcc phase. Increasing the holding time during sintering is useful to ensure the complete transition of phases [29].

3.6. Microhardness analysis

Fig. 6 shows the microhardness results of SPSed $Al_{20}Cr_{20}Fe_{25}Ni_{25}Mn_{10}$ alloy and post-heat treatment. The figure reveals the increased microhardness of the alloy as a function of the increased sintering temperature and holding time. Prior to heat treatment, the SPSed alloys showed optimal and minimum microhardness values of HV 447.97 and HV 120.9, respectively. The maximal microhardness was an outcome of the fabrication of $Al_{20}Cr_{20}Fe_{25}Ni_{25}Mn_{10}$ at high sintering temperature (1000°C) and prolonged holding time (12 min), whereas the lowest microhardness was linked with low sintering temperature (800°C) and short holding time (12 min). Such outcome can possibly be attributed to the presence of high-intensity AlCr and AlNi hard intermetallic phases, densification, and severe lattice distortion. The bcc hard phases formed at elevated temperatures, and they exhibited a superior hardening effect over fcc [4]. High density, which is associated with high sintering temperature and prolonged holding time (Fig. 1), played a significant contributory role in hardness enhancement [33]. On the other hand, lattice distortion, which prompted grain boundary pinning, intensified with the increase in sintering temperatures and holding times given that the movement of atoms became more pronounced [4]. Thus, after heat treatment, the alloys' microhardness significantly increased, except for that of two alloys that were sintered at temperature of 1000°C and holding times of 8 and 12 min. Fig. 7 shows further details on the alloys.

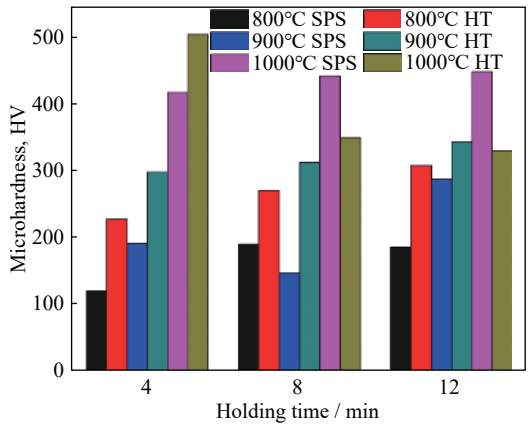

Fig. 6. Comparative microhardness graph of SPS and heat-treated (HT) sintered $Al_{20}Cr_{20}Fe_{25}Ni_{25}Mn_{10}$ alloys.

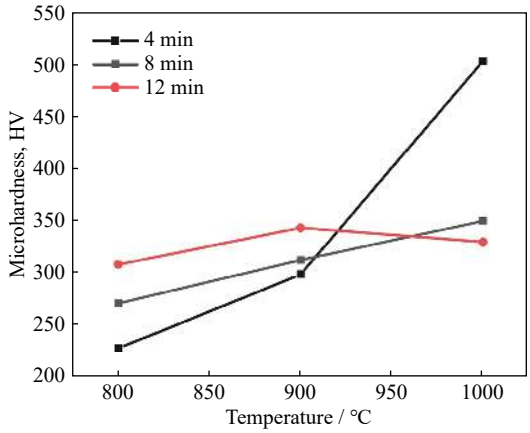

Fig. 7. Influence of heat treatment temperature on the microhardness of the SPSed alloys.

Fig. 7 presents the results of measured microhardness of SPSed alloys HT at different temperatures. Noteworthy, the heat treatment at temperatures of 800°C and 900°C resulted in microhardness increase compared with the untreated SPSed alloy (Fig. 6). The significance of heat treatment was quantified by demonstration, that is, with the increment from HV 120.9 to HV 227.4 for the alloy that had the lowest microhardness among all SPSed alloys before heat treatment. Microhardness improvement caused by heat treatment was possibly due to the controlled cooling rate and recrystallization of deformed grains. Heat treatment of HEAs composed of supersaturated or inhomogeneous phases improved the phase distribution [18]. On the other hand, instead of continual microhardness increment, as the heat treatment temperature rose to 1000°C, a substantial decline in microhardness from HV 447.97 to HV 329.47 was observed for SPSed alloy, portraying maximal microhardness prior to heat treatment (Fig. 7). Fig. 7 reveals that this trend of decreased microhardness transpired for SPSed alloys fabricated at 8 and 12 min and 1000°C sintering temperature.

By contrast, the increase in microhardness after heat treat-

ment witnessed on $Al_{20}Cr_{20}Fe_{25}Ni_{25}Mn_{10}$ alloys fabricated at 1000°C with 8 and 12 min holding time can be attributed to the disordered bcc phase, which transformed into an ordered crystal structure, present in $Al_{20}Cr_{20}Fe_{25}Ni_{25}Mn_{10}$ alloy [29]. Another possible explanation for the decrease in microhardness can be the interaction of high content Al with one or three elements during SPS fabrication at high temperatures and prolonged sintering times, thereby probably forming traces of B2 phase that could not be detected by XRD. This phase is a bcc phase that exhibited high hardness and formed as a result of high Al contents [19]. Subjection of such alloys to heat treatment caused the homogenization of phases within the alloy's matrix, thereby suppressing the hardness effect induced by B2 phase.

3.7. Electrochemical studies

3.7.1. Potentiodynamic polarization analysis

Figs. 8–10 present the potentiodynamic polarization curves of $Al_{20}Cr_{20}Fe_{25}Ni_{25}Mn_{10}$ alloys at various parameters in 0.5 M H_2SO_4 medium. Varying of sintering parameters showed a significant effect on the corrosion behavior of the developed alloys. With regard to the comparisons of varying holding times, the best current densities were observed at a holding time of 8 min at 900°C (Fig. 9) and 12 min at 800°C (Fig. 8) and 1000°C (Fig. 10). The alloys sintered at 12 min holding time at 800°C and 1000°C showed a high potential over alloys sintered at lower 4 and 8 min holding time. Comparatively, the alloys fabricated at 1000°C and 12 min holding time outperformed those sintered at 800°C and 900°C. Notably, temperature showed a significant influence given the wide margin of difference between the current densities of alloys fabricated at different temperatures and at 12 min holding time compared with those at varying holding times (Figs. 8–10). A low current density implies a low corrosion resistance. Meanwhile, a high potential indicates a high passivity. The improved corrosion performance exhibited by the alloy sintered at 1000°C with 12 min holding time can be attributed to the maximal densification of the alloy (Fig. 1).

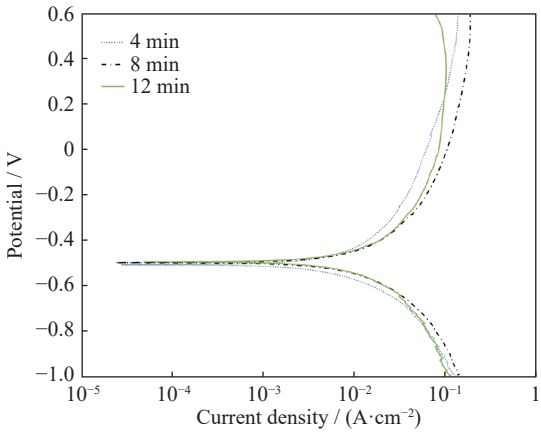

Fig. 8. Polarization curves of the alloy sintered at 800°C.

The corrosion behavior can be swayed into a positive outcome due to the high densification that reduces porosity and volume defects [5]. In contrast to densification, porosity

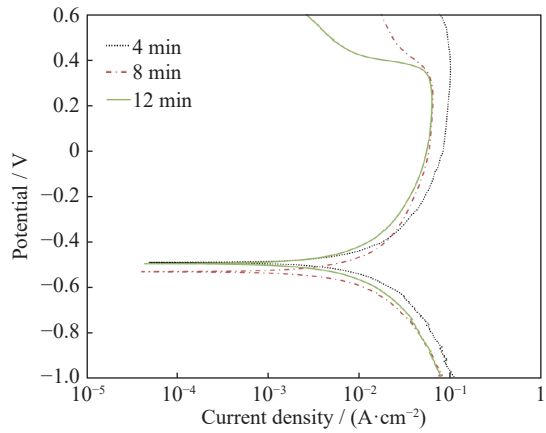

Fig. 9. Polarization curves of the alloy sintered at 900°C.

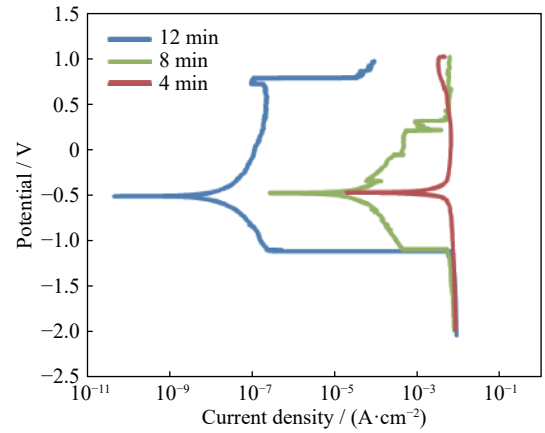

Fig. 10. Polarization curves of the alloy sintered at 1000°C.

renders an alloy susceptible to corrosion attacks because pores are vicinities where electrolyte accumulates [34]. Variation in the microstructures present in the alloys can be another reason. Corrosion sites tend to form on grain boundaries [35]. From the above point, most grain boundaries exhibited by alloys fabricated at low sintering holding time and temperature led to poor corrosion performance. A high potential means the capability to be passive in corrosive medium, whereas the formation of oxide layers prompts a high passivity. The high potential portrayed by the alloys fabricated at 12 min holding time can be ascribed to the high compactness of Cr atoms present in the alloy. The high-concentration Cr forms a protective oxide layer against corrosion attacks in oxygenated environments [36]. In the equiatomic AlCrFeMnNi HEA observed by Masemola *et al.* [37], Cr was an active element that formed a passive oxide film when subjected to sulfuric acid solution.

With regard to the comparison between the significance caused by temperature and holding time on corrosion behavior of the alloys, the increase in temperature decreased the current density, whereas the holding time exhibited no distinct relationship with the current density of the alloys. The scientific reasoning behind this outcome cannot be found in literature. However, in theory, sintering at 900°C at 8 and 12 min holding times did not cause considerable microstructural changes, which subsequent plays a role in the electrochemical properties of the alloys. The $Al_{20}Cr_{20}Fe_{25}Ni_{25}Mn_{10}$ alloy

produced at 1000°C and 12 min holding time showed superior corrosion performance. The increase in temperature during sintering showed a prominent influence on the chemical behavior of the alloys [38].

3.7.2. SEM of corroded alloys

Fig. 11(a)–(c) shows the SEM micrographs of $Al_{20}Cr_{20}Fe_{25}Ni_{25}Mn_{10}$ alloys sintered at 800°C with different holding times after corrosion testing. The micrographs revealed the presence of white and dark structures. The black structures were superior in numbers over the white ones for the alloys sintered at 4 and 8 min holding times, whereas the alloy sintered at 12 min contained less quantity of black structures. As referred from Fig. 8, the potentiodynamic polarization curve of the alloys sintered at the above-mentioned holding times performed poorly in comparison with the alloy developed at 12 min.

The surface of sample produced at 12 min (Fig. 3(c)), which showed superior corrosion resistance over the other samples fabricated at 800°C, exhibited minimal dark phases. The surface of $Al_{20}Cr_{20}Fe_{25}Ni_{25}Mn_{10}$ alloy sintered at 800°C with 8 min holding time (Fig. 11(b)) revealed more black phases and the poorest performance in terms of corrosion behavior in 0.5 M H_2SO_4 medium. This finding illustrates that the black phases can be the products of corrosion. Thus, corrosion was probably not prevented from further commencing because of such instabilities.

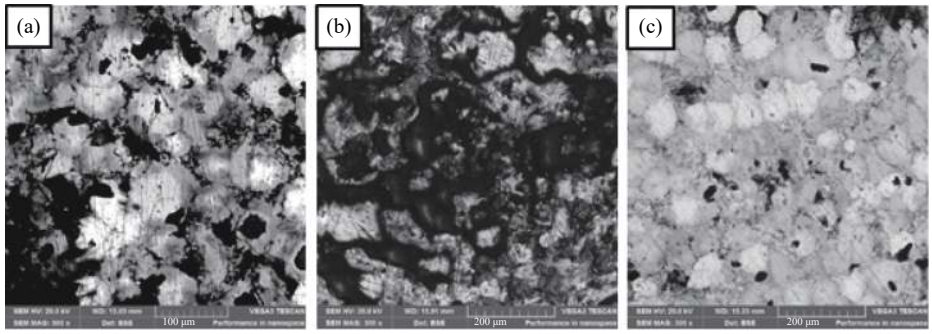

Fig. 11. SEM results of the alloys sintered at 800°C after corrosion for (a) 4, (b) 8, and (c) 12 min.

4. Conclusions

A non-equiatomic AlCrFeNiMn alloy was fabricated by using SPST to understand the structures (fcc or bcc) present in the alloy. The effects of sintering temperature and holding time on the microstructural evolution, densification, microhardness, and corrosion behavior of the developed HEAs were investigated, and the following conclusions were drawn.

(1) High density alloys were synthesized, with the optimal densification of 99.6% achieved at 1000°C and a holding time of 12 min. This result indicates that a dense $Al_{20}Cr_{20}Fe_{25}Ni_{25}Mn_{10}$ alloy can be plausibly fabricated using SPST.

(2) Elemental analysis quantified by EDS confirms that all the elements selected in this paper were present in the alloy produced.

(3) SEM showed no significant evidence of cracks and pores, supporting the achievement of highly dense SPSed alloys.

(4) XRD, EDS, and SEM collectively provided proof that the globular microstructures in $Al_{20}Cr_{20}Fe_{25}Ni_{25}Mn_{10}$ alloy was a fcc solid solution (HEA) synthesized at temperatures lower than the average calculated melting point of $Al_{20}Cr_{20}Fe_{25}Ni_{25}Mn_{10}$.

(5) The maximum microhardness of HV 447.97 was achieved at a sintering temperature of 1000°C and a holding time of 12 min. After heat treatment, the microhardness decreased from HV 447.97 to HV 329.47 due to the disordered phases transforming into ordered crystal structure. However, no distinct relationship was observed between the microhardness improvements of sintered alloys with heat treatment.

(6) A similar alloy that showed superior microhardness portrayed outstanding corrosion resistance properties over the other SPSed alloys.

(7) An increase in sintering temperature during SPSed of $Al_{20}Cr_{20}Fe_{25}Ni_{25}Mn_{10}$ HEA yielded better densification, high microhardness, and superior corrosion resistance in 0.5 M H_2SO_4.

Acknowledgements

The authors acknowledge the support from Institute for Nano-Engineering Research and Surface Engineering Research Centre of Tshwane University of Technology and National Research Foundation of South Africa, Pretoria, South Africa.

Conflict of Interest

The authors declare no conflict of interest.

References

[1] B.S. Murty, J.W. Yeh, and S. Ranganathan, A brief history of alloys and the birth of high-entropy alloys, [in] *High Entropy Alloys*, Amsterdam: Elsevier, 2014, p. 1.

[2] J.W. Yeh, S.K. Chen, S.J. Lin, J.Y. Gan, T.S. Chin, T.T. Shun, C.H. Tsau, and S.Y. Chang, Nanostructured high-entropy alloys with multiple principal elements: Novel alloy design concepts and outcomes, *Adv. Eng. Mater.*, 6(2004), No. 5, p. 299.

[3] J.W. Yeh, Recent progress in high-entropy alloys, *Ann. Chim.*

Sci. Mat., 31(2006), No. 6, p. 633.
[4] L. Rudolf Kanyane, A. Patricia Popoola, and N. Malatji, Development of spark plasma sintered TiAlSiMoW multicomponent alloy: Microstructural evolution, corrosion and oxidation resistance, *Results Phys.*, 12(2019), p. 1754.
[5] N. Malatji, A.P.I. Popoola, T. Lengopeng, and S. Pityana, Tribological and corrosion properties of laser additive manufactured AlCrFeNiCu high entropy alloy, *Mater. Today: Proc.*, 28(2020), p. 944.
[6] K.K. Alaneme, M.O. Bodunrin, and S.R. Oke, Processing, alloy composition and phase transition effect on the mechanical and corrosion properties of high entropy alloys: A review, *J. Mater. Res. Technol.*, 5(2016), No. 4, p. 384.
[7] L.C. Tsao, C.S. Chen, and C.P. Chu, Age hardening reaction of the $Al_{0.3}CrFe_{1.5}MnNi_{0.5}$ high entropy alloy, *Mater. Des.* (*1980-2015)*, 36(2012), p. 854.
[8] S. Guo, C. Ng, J. Lu, and C.T. Liu, Effect of valence electron concentration on stability of fcc or bcc phase in high entropy alloys, *J. Appl. Phys.*, 109(2011), No. 10, art. No. 103505.
[9] Z.Q. Fu, W.P. Chen, H.M. Wen, Z. Chen, and E.J. Lavernia, Effects of Co and sintering method on microstructure and mechanical behavior of a high-entropy $Al_{0.6}NiFeCrCo$ alloy prepared by powder metallurgy, *J. Alloys Compd.*, 646(2015), p. 175.
[10] S.Y. Zhang, X.F. Zhang, Q.S. Lu, P. He, T.S. Lin, and H.Y. Geng, Investigation of melt-spinning speed on the property of $Yb_{0.2}Ba_{0.1}Al_{0.1}Ga_{0.1}In_{0.1}La_{0.05}Eu_{0.05}Co_{3.75}Fe_{0.25}Sb12$ skutterudites, *Mater. Lett.*, 260(2020), art. No. 126960.
[11] S.Y. Zhang, S.W. Xu, H. Gao, Q.S. Lu, T.S. Lin, P. He, and H.Y. Geng, Characterization of multiple-filled skutterudites with high thermoelectric performance, *J. Alloys Compd.*, 814(2020), art. No. 152272.
[12] G. Popescu, M.M. Adrian, I. Csaki, C.A. Popescu, D. Mitrică, S. Vasile, and I. Carcea, Mechanically alloyed high entropy composite, *IOP Conf. Ser.: Mater. Sci. Eng.*, 145(2016), No. 7, art. No. 072007.
[13] S. Varalakshmi, M. Kamaraj, and B.S. Murty, Synthesis and characterization of nanocrystalline AlFeTiCrZnCu high entropy solid solution by mechanical alloying, *J. Alloys Compd.*, 460(2008), No. 1-2, p. 253.
[14] C.S. Babu, K. Sivaprasad, V. Muthupandi, and J.A. Szpunar, Characterization of nanocrystalline AlCoCrCuNiFeZn high entropy alloy produced by mechanical alloying, *Procedia Mater. Sci.*, 5(2014), p. 1020.
[15] S. Riva, S.G.R. Brown, N.P. Lavery, A. Tudball, and K.V. Yusenko, Spark plasma sintering of high entropy alloys, [in] P. Cavaliere, eds., *Spark Plasma Sintering of Materials*, Springer, Cham, 2019, p. 517.
[16] S. Yadav, K. Biswas, and A. Kumar, Spark plasma sintering of high entropy alloys, [in] P. Cavaliere, eds., *Spark Plasma Sintering of Materials*, Springer, Cham, 2019, p. 539.
[17] Y.F. Ye, Q. Wang, J. Lu, C.T. Liu, and Y. Yang, High-entropy alloy: Challenges and prospects, *Mater. Today*, 19(2016), No. 6, p. 349.
[18] J.F. Zeng, C.J. Wu, H.P. Peng, Y. Liu, J.H. Wang, and X.P. Su, Microstructure and microhardness of as-cast and 800 ℃ annealed $Al_xCr_{0.2}Fe_{0.2}Ni_{0.6-x}$ and $Al_{0.2}Cr_{0.2}Fe_yNi_{0.6-y}$ alloys, *Vacuum*, 152(2018), p. 214.
[19] A. Munitz, L. Meshi, and M.J. Kaufman, Heat treatments' effects on the microstructure and mechanical properties of an equiatomic Al–Cr–Fe–Mn–Ni high entropy alloy, *Mater. Sci. Eng. A*, 689(2017), p. 384.
[20] D. Choudhuri, B. Gwalani, S. Gorsse, C.V. Mikler, R.V. Ramanujan, M.A. Gibson, and R. Banerjee, Change in the primary solidification phase from fcc to bcc-based B2 in high entropy or complex concentrated alloys, *Scr. Mater.*, 127(2017), p. 186.
[21] A.J. Zhang, J.S. Han, J.H. Meng, B. Su, and D.L. Pen, Rapid preparation of AlCoCrFeNi high entropy alloy by spark plasma sintering from elemental powder mixture, *Mater. Lett.*, 181(2016), p. 82.
[22] N. Eißmann, B. Klöden, T. Weißgärber, and B. Kieback, High-entropy alloy CoCrFeMnNi produced by powder metallurgy, *Powder Metall.*, 60(2017), No. 3, p. 184.
[23] R.M. German, Coarsening in sintering: Grain shape distribution, grain size distribution, and grain growth kinetics in solid-pore systems, *Crit. Rev. Solid State Mater. Sci.*, 35(2010), No. 4, p. 263.
[24] S. Wagner, D. Kahraman, H. Kungl, M.J. Hoffmann, C. Schuh, K. Lubitz, H. Murmann-Biesenecker, and J.A. Schmid, Effect of temperature on grain size, phase composition, and electrical properties in the relaxor-ferroelectric-system $Pb(Ni_{1/3}Nb_{2/3})O_3$–$Pb(Zr, Ti)O_3$, *J. Appl. Phys.*, 98(2005), No. 2, art. No. 024102.
[25] S. Kennedy, S. Kumaran, and T. Srinivasa Rao, Microstructure and mechanical properties of γ-TiAl consolidated by spark plasma sintering, *Integr. Ferroelectr.*, 185(2017), No. 1, p. 11.
[26] A.V. Adedayo, Development processes of globular microstructure, *J. Miner. Mater. Charact. Eng.*, 10(2011), No. 7, p. 651.
[27] A.G. Atkins, Deformation-mechanism maps (the plasticity and creep of metals and ceramics), *J. Mech. Work. Technol.*, 9(1984), No. 2, p. 224.
[28] S. Elkatatny, M.A.H. Gepreel, A. Hamada, K. Nakamura, K. Yamanaka, and A. Chiba, Effect of Al content and cold rolling on the microstructure and mechanical properties of $Al_5Cr_{12}Fe_{35}Mn_{28}Ni20$ high-entropy alloy, *Mater. Sci. Eng. A*, 759(2019), p. 380.
[29] M.H. Xiao, J.W. Chen, J.J. Kang, K. Chen, D. Wu, and N. Gao, Effect of heat treatment process on mechanical properties and microstructure of $FeAlCoCrNiTi_{0.5}$ alloy, *AIP Adv.*, 8(2018), No. 9, art. No. 095322.
[30] B. Ren, Z.X. Liu, D.M. Li, L. Shi, B. Cai, and M.X. Wang, Effect of elemental interaction on microstructure of CuCrFeNiMn high entropy alloy system, *J. Alloys Compd.*, 493(2010), No. 1-2, p. 148.
[31] Y.P. Wang, B.S. Li, and H.Z. Fu, Solid solution or intermetallics in a high-entropy alloy, *Adv. Eng. Mater.*, 11(2009), No. 8, p. 641.
[32] R.B. Li, W.W. Zhang, Y. Zhang, and P.K. Liaw, The effects of phase transformation on the microstructure and mechanical behavior of $FeNiMnCr_{.75}Al_x$ high-entropy alloys, *Mater. Sci. Eng. A*, 725(2018), p. 138.
[33] B.J. Babalola, N. Maledi, M.B. Shongwe, M.O. Bodunrin, B.A. Obadele, and P.A. Olubambi, Influence of nanocrystalline nickel powder on oxidation resistance of spark plasma sintered Ni–17Cr6.5Co1.2Mo6Al4W7.6Ta alloy, *J. King Saud Univ. Eng. Sci.*, 32(2020), No. 3, p. 198.
[34] A. Mthisi and A.P.I. Popoola, Influence of Al_2O_3 addition on the hardness and *in vitro* corrosion behavior of laser synthesized Ti–Al_2O_3 coatings on Ti–6Al–4V, *Int. J. Adv. Manuf. Technol.*, 100(2019), No. 1-4, p. 917.
[35] R.N. Lumley, Fundamentals of aluminium metallurgy: production, processing, and applications, [in] N. Birbilis and B. Hinton, eds., *Corrosion and Corrosion Protection of Aluminium*, Woodhead Publishing, Oxford, 2011, p. 574.
[36] T.M. Butler and M.L. Weaver, Oxidation behavior of arc melted AlCoCrFeNi multi-component high-entropy alloys, *J. Alloys Compd.*, 674(2016), p. 229.
[37] K. Masemola, P. Popoola, and N. Malatji, The effect of annealing temperature on the microstructure, mechanical and electrochemical properties of arc-melted AlCrFeMnNi equi-atomic High entropy alloy, *J. Mater. Res. Technol.*, 9(2020), No. 3, p. 5241.
[38] L.R. Kanyane, N. Malatji, A.P.I. Popoola, and M.B. Shongwe, Evolution of microstructure, mechanical properties, electrochemical behaviour and thermal stability of $Ti_{0.25}$–$Al_{0.2}$–$Mo_{0.2}$–$Si_{0.25}W_{0.1}$ high entropy alloy fabricated by spark plasma sintering technique, *Int. J. Adv. Manuf. Technol.*, 104(2019), No. 5-8, p. 3163.